RSC Applied Interfaces

Accepted Manuscript

This article can be cited before page numbers have been issued, to do this please use: C. M. Avinash, C. Nethravathi and M. Rajamathi, *RSC Appl. Interfaces*, 2026, DOI: 10.1039/D6LF00195E.

ROYAL SOCIETY OF CHEMISTRY

rsc.li/RSCApplInter

View Article Online
DOI: 10.1039/D6LF00195E

ARTICLE

α and β–motifs Interstratified β_{bc}–Nickel Hydroxide for Enhanced OER and UOR Electrocatalysis

Received 00th January 20xx,
Accepted 00th January 20xx

DOI: 10.1039/x0xx00000x

C. M. Avinash,[a] C. Nethravathi*[a,b] and Michael Rajamathi*[a]

Nickel hydroxide presents itself in a variety of interesting polymorphic modifications. One such polymorphic form, β_{bc}–nickel hydroxide, is known to be a poorly ordered solid in which α (~15%) and β motifs are interstratified. The α/β interfaces propel the reconstruction of β_{bc} to Ni^{4+} containing γ-nickel oxyhydroxide, a process kinetically hindered in the case of pristine ordered β-phase. Defect-rich γ-nickel oxyhydroxide with a high ECSA, boosts electronic conductivity and accelerates charge transfer to drive enhanced oxygen evolution reaction (OER) kinetics delivering higher current densities at lower potentials. β_{bc}–phase outperforms β–nickel hydroxide in OER with lower onset potential (β_{bc} = 1.5 V_{RHE} compared to β = 1.55 V_{RHE}), higher current density and lower Tafel slope (β_{bc} = 60 mV dec^{-1} compared to β = 95 mV dec^{-1}). The β_{bc} polymorph also efficiently catalyses urea oxidation reaction (UOR) with a sustained Ni^{3+}/Ni^{4+} active surface delivering an onset potential of 1.35 V_{RHE} and a Tafel slope of 25 mV dec^{-1}.

1. Introduction

Nickel hydroxide[1-3] has been studied in the past for its application as electrode material in alkaline secondary storage batteries[4,5] and supercapacitors.[6,7] Nickel hydroxide crystallizes in a variety of polymorphic phases with the major ones being β–nickel hydroxide and α–nickel hydroxide.[1-3,8,9] The β–form is a stoichiometric compound with the formula $Ni(OH)_2$ and is isostructural with the mineral brucite [$Mg(OH)_2$, hexagonal, $P\bar{3}m1$] while the α-phase is hydroxyl deficient due to partial protonation of the hydroxyl groups resulting in layers of composition $[Ni(OH)_{2-x}(H_2O)_x]^{x+}$ leading to the intercalation of charge compensating anions in the interlayer region.[1-3,8,9] In addition to these, a number of phases, in which the β and α motifs are interstratified are known.[1-3,8,9] These are now labelled IS–nickel hydroxide.[1-3,8,9] When the percentage of the interstratified α–motifs is low (<20%), the XRD pattern of the sample resembles that of β–nickel hydroxide except for peak broadening of select reflections.[8,9] This phase is called β_{bc}–nickel hydroxide.[8]

The electrochemical performance of nickel hydroxide is related to its polymorphic form.[1,3,4,10] In alkaline secondary storage battery application, the β–form cycles between β–nickel hydroxide and β–nickel oxyhydroxide (NiOOH) with charge storage per nickel atom being $1e^-$.[1,4] The α–form cycles between α–nickel hydroxide and γ–nickel oxyhydroxide (H_xNiO_2, x = 0.25-0.3) with the charge storage capacity being $1.7e^-$ per nickel atom.[1,4] However, the α–phase is unstable in the alkaline medium of the battery, limiting its application as the electrode material.

There is a renewed interest in layered nickel hydroxide for its potential application as an electrocatalyst in oxygen evolution reaction (OER),[11] the anodic reaction during the electrolysis of water. The general focus[12] has been in nano-structuring[13-16] and hybridization[17,18] of nickel hydroxide with other materials in addition to doping with other metals[19,20] to improve the catalytic efficiency.

When nickel hydroxide is used as the electrocatalyst,[11] the active catalytic material for OER is nickel oxyhydroxide,[11,21,22] as OER is observed after the oxidation of Ni^{2+} to Ni^{3+} (1.37 V_{RHE}, 1 M KOH). OER occurs at potentials (> 1.5 V_{RHE}) far higher than the potential (1.37 V_{RHE}) at which β-nickel oxyhydroxide, NiOOH, is formed. At such high potentials β–nickel oxyhydroxide is expected to overcharge leading to the formation of γ–nickel oxyhydroxide, H_xNiO_2 (x ≈ 0.33), containing ~33% Ni^{3+} and ~66% Ni^{4+}. Thus, the active catalytic species for OER could be either γ-oxyhydroxide or both β- and γ–oxyhydroxides. While α-nickel hydroxide that readily forms γ–oxyhydroxide shows promising OER catalytic activity, its structural instability in the alkaline medium makes it a poor choice for sustainable use.

Nickel-based layered double hydroxides (LDH),[11] specifically NiFe-LDH, with tuneable electronic structure and active sites are coveted catalytic materials for electrocatalytic OER. Lattice distortions, cation vacancies, or anion mediated modulation of hydroxide layer charge density promote low oxidization potential, accelerated limiting process and enhanced proton/electron transfer kinetics.[11, 23] Despite these merits, Fe

[a] Materials Research Group, St. Joseph's University, Bangalore 560027, India. michael.rajamathi@sju.edu.in
[b] Department of Chemistry, Mount Carmel College, Bangalore 560001, India. nethravathic@gmail.com

Electronic Supplementary Information (ESI) available: [LSV data without IR correction, CV, UOR electrochemical data for β–nickel hydroxide and Tables comparing the performance of β_{bc}–nickel hydroxide with related electrocatalysts reported in the literature]. See DOI: 10.1039/x0xx00000x

View Article Online DOI: 10.1039/D5LF00105E

leaching in alkaline electrolyte causes rapid deactivation and decreased electronic conductivity.[23] The oxidation of interlayer anions release gases and protons which hasten layer collapse and worsen pH fluctuations.[23] Thus, it is important to seek robust Ni-based materials to sustain structural integrity under operational conditions and conserve catalytic activity.

Mixed polymorphic materials have been shown to deliver augmented catalytic activity in diverse reactions. For example, the high activity of Degussa, a commercial photocatalyst, is attributed to the synergistic interaction between rutile and anatase polymorphs of TiO_2.[24] Similarly, 1T/2H mixed polymorphic MoS_2 displays higher catalytic activity than its pristine 2H-phase.[25] Improved electrocatalytic HER has been observed at hexagonal/monoclinic WO_3 phase junctions.[26]

In this context, it would be interesting to probe the mixed polymorphic nickel hydroxide phases as potential electrocatalysts towards small molecule oxidation with enhanced stability and maximum active nickel content. Among the interstratified phases, β_{bc}–nickel hydroxide with a modest 10-15% α-motifs is quite stable in alkaline medium. As the α-motifs in β_{bc} polymorph oxidize directly to γ–oxyhydroxide, this phase is expected to catalyse OER better than β–nickel hydroxide, if the γ–oxyhydroxide is indeed the active catalytic species.

This work explores the relative performances of β and β_{bc}–nickel hydroxide as electrocatalyst for OER and UOR. X-ray diffraction and photoelectron spectroscopy of the spent electrodes identifies the active catalytic species to be γ–oxyhydroxide in OER and β–oxyhydroxide in the case of UOR.

2. Experimental Section

2.1 Synthesis of β–nickel hydroxide

β–nickel hydroxide was obtained by dropwise addition of 50 mL of 1M nickel nitrate solution into 50 mL of 2M NaOH solution with constant stirring at room temperature.[8] The resulting gel so obtained was hydrothermally treated in a Teflon lined autoclave at 180 ^{o}C for 48 h. The product was washed with deionized water and dried at 65 ^{o}C.

2.2 Synthesis of β_{bc}– nickel hydroxide

β_{bc}–nickel hydroxide was obtained by dropwise addition of 50 mL of 2 M NaOH solution into 50 mL of 1 M nickel nitrate solution with constant stirring at room temperature.[8] The product was washed with deionized water and dried at 65 ^{o}C.

2.3 Characterization

All the solid products were characterized by powder X-ray diffraction (XRD) using a PANalytical X'pert PRO diffractometer (Cu Kα, λ = 1.5418 Å) fitted with a secondary graphite monochromator. Diffraction patterns were recorded from 5° to 70°, with a step size of 0.020° and time per step of 2.4 s. The powder samples were loaded on a quartz sample holder to record the XRD data. The infrared (IR) spectra of the samples were recorded using a PerkinElmer Spectrum Two FTIR spectrometer operated in the ATR mode, in the range of 4000–550 cm^{-1} with 4 cm^{-1} resolution. The Raman spectra of the samples were recorded on HORIBA Jobin-Yvon LabRAM HR800 at 532 nm excitation wavelength. Scanning electron microscopy (SEM) images were recorded using a Zeiss, Ultra 55 field emission scanning electron microscope. Transmission electron microscopy (TEM) images were acquired with a Titan 300 Themis operated at 300 kV. Thermogravimetric (TG) analysis was carried out using PerkinElmer STA 6000. The sample (~3 mg) was loaded in a 250-µL alumina crucible and heated from 30 to 700 °C under nitrogen flow (20 mL min^{-1}) at a ramping rate of 5 °C min^{-1}. Nickel content in the samples was estimated by gravimetry.

2.4 Electrochemical measurements

Electrochemical measurements were recorded using Metrohm Autolab (PGSTAT204) electrochemical workstation. The experiments were performed in a three-electrode cell employing graphite sheet loaded with the catalyst, Pt and Ag/AgCl as working, counter and reference electrodes respectively. While oxygen evolution reactions were recorded in 1M KOH as electrolyte, urea oxidation was carried out in 1M KOH solution containing 0.33M of urea. The homogeneous catalyst ink was prepared by grinding 20 mg of β/β_{bc}–nickel hydroxide in 500 µL isopropyl alcohol and 100 µL nafion (5%). Subsequently the ink was coated on a 1 x 1 cm graphite sheet of 0.5 mm thickness and dried at room temperature overnight. Cyclic voltammetry (CV) and linear sweep voltammetry (LSV) were recorded in the potential range -0.6/0.0 to 1V (vs Ag/AgCl). The LSV data are presented after 85% IR compensation.[27] The uncorrected data are presented in supplementary information (SI, Figure S1). The Nyquist plots were measured by applying a frequency range 0.1 to 0.7783 Hz and a potential of 1.5 V (vs RHE). Chronoamperometry measurements were recorded for OER and UOR at 1.675 V and 1.40 V (vs RHE) respectively.

2.5 Characterization of the spent electrodes

The spent electrodes were removed from the cell, rinsed with water, dried and subjected to characterization by XRD and X-ray photoelectron spectroscopy (XPS) analysis (Kratos Analytical, Axis Supra^{+}) to identify the nature of the Ni species at the potential at which the catalytic reactions were conducted. The electrodes were subjected to various reaction conditions such as cyclic voltammetry, single sweep LSV and chronoamperometry for various time periods ranging from 15 minutes to 4 hours.

3. Results and Discussion

The chemical compositions of the as prepared samples verified from nickel content and thermogravimetric analysis (Figure 1A) are $Ni(OH)_2$ (β–phase) and $Ni(OH)_{1.98}(NO_3)_{0.07}{\cdot}0.54H_2O$ (β_{bc}–phase).

View Article Online
DOI: 10.1039/D6LF00195E

ARTICLE

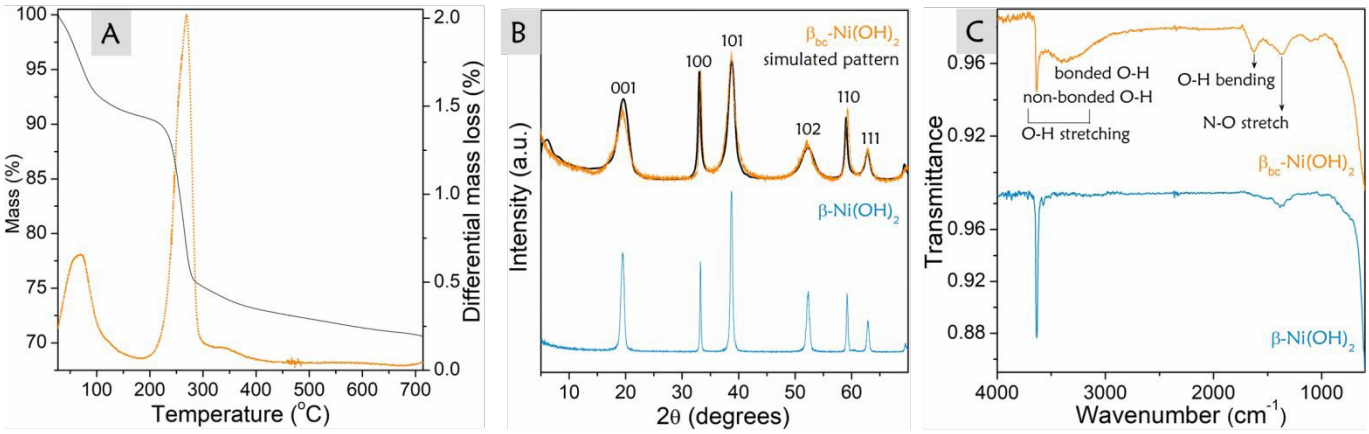

Figure 1 TG (–) and DTG(...) curves of β_{bc}–nickel hydroxide (A); XRD patterns (B) and IR spectra (C) of β–nickel hydroxide and β_{bc}–nickel hydroxide. The DiFFax simulated pattern is overlaid on the XRD pattern of β_{bc}–nickel hydroxide in panel B.

Table 1 Comparison of powder X-ray diffraction data of β and β_{bc}–nickel hydroxide phases

hkl	d (Å)		FWHM (rad)	
	β	β_{bc}	β	β_{bc}
001	4.55	4.56	0.0125	0.0457
100	2.696	2.691	0.0043	0.0096
101	2.326	2.327	0.0082	0.0318
102	1.749	1.753	0.0109	0.0365
110	1.561	1.559	0.0057	0.0126
111	1.478	1.478	0.0077	0.0171

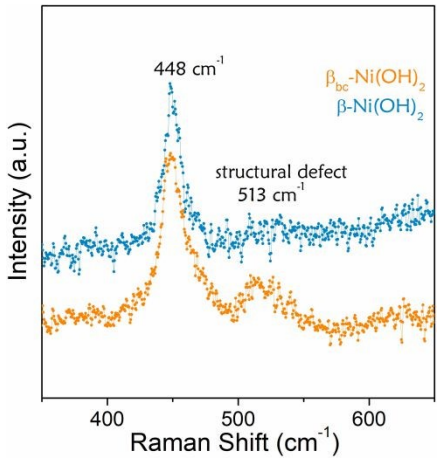

Figure 2 Raman spectra of β and β_{bc}–nickel hydroxide.

The XRD patterns of the as prepared β and β_{bc}–phases of nickel hydroxide are shown in Figure 1B. Table 1 summarizes the reflections of β and β_{bc}–phases and these are similar to the observations recorded in our earlier work.[9] Although both the phases show reflections with comparable d-spacings, the β–phase is characterized by sharp reflections while the β_{bc}–phase exhibits both broad and sharp reflections. Broad non-*hk*0 reflections in the β_{bc}–phase is due to poorly defined c-parameter arising from the interstratification with a small percentage of α–motifs and the resultant disordered stacking of layers (Figure 2).[8,9]

In our previous work[8], DIFFaX[28] a software best suited to study stacking disorders in layered solids, was employed to simulate the XRD pattern of various IS-nickel hydroxide phases. Here, the DIFFaX simulated pattern with 12% α-motif interstratification (simulation conditions are described in the Supplementary Information) matches well with observed pattern of β_{bc}– nickel hydroxide (Figure 1B). The α-motif content arrived at from the simulation studies corroborates with ~15% content indicated by the composition analysis.

The existence of the interstratified phase[8,9] is further corroborated by IR (Figure 1C) and Raman spectroscopy (Figure 2). The β–phase (Figure 1C) is characterized by a sharp absorption at 3650 cm^{-1} due to the non-hydrogen bonded hydroxyl groups and the absence of any anion related absorptions in the range 1500-1000 cm^{-1}. In contrast, the β_{bc}–phase (Figure 1C) exhibits a weak broad (3382 cm^{-1}) and sharp (3630 cm^{-1}) absorptions due to the hydrogen bonded and non-hydrogen bonded hydroxyl groups respectively and an antisymmetric stretching absorption (1368 cm^{-1}) due to the intercalated C_{2v} nitrate ions. These features confirm the incorporation of α–motifs in β_{bc}–nickel hydroxide. As observed by Bernard et al.,[29] Raman spectra of both β and β_{bc}–nickel hydroxide (Figure 2), exhibit Ni-O stretching vibrations at 448 cm^{-1}. In addition, β_{bc}–nickel hydroxide reveals a peak at ~513 cm^{-1} due to structural defects characteristic of the β_{bc} phase.

The morphology of the nickel hydroxide polymorphs was examined using scanning electron microscopy (Figure 3). While the SEM image of β–nickel hydroxide (Figure 3a) exhibits uniform hexagonal platelets of ~200 nm in size, β_{bc}–nickel hydroxide consists of nanostructures that are ~20-30 nm in size (Figure 3b). The TEM

image of β_{bc}–nickel hydroxide nanostructures (Figure 3c) reveal that the sample is composed of thin, transparent layers of lateral size less than 50 nm. When viewed through the crystallite edge (Figure 3d), the lattice fringes of 4.6 Å corresponding to β–nickel hydroxide are observed largely along with a few regions of 8.6 Å corresponding to the α–motifs confirming the existence of α and β motifs in β_{bc}–nickel hydroxide.

View Article Online DOI: 10.1039/D0LF00125F

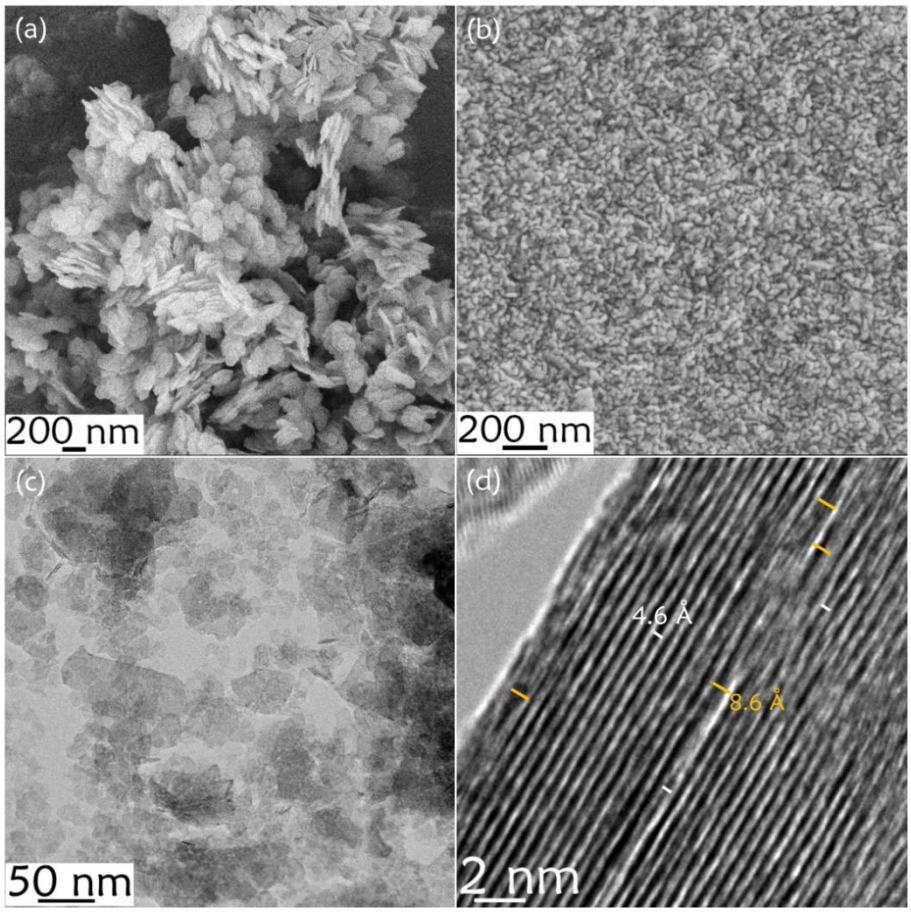

Figure 3 SEM images of β–nickel hydroxide (a) and β_{bc}–nickel hydroxide (b). Bright field TEM image (c) and HRTEM image (d) of a crystallite edge of β_{bc}–nickel hydroxide.

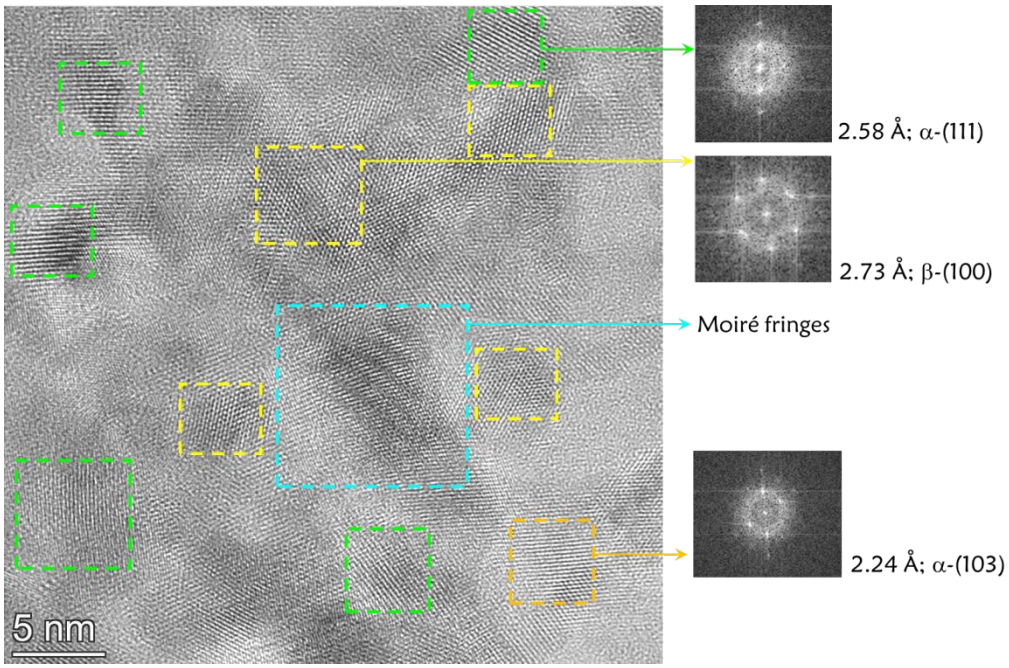

Figure 4 In-plane HRTEM image and Fast Fourier Transform (FFT) analysis of β_{bc}–nickel hydroxide reveal the existence of α-β junctions.

View Article Online
DOI: 10.1039/D6LF00195E

ARTICLE

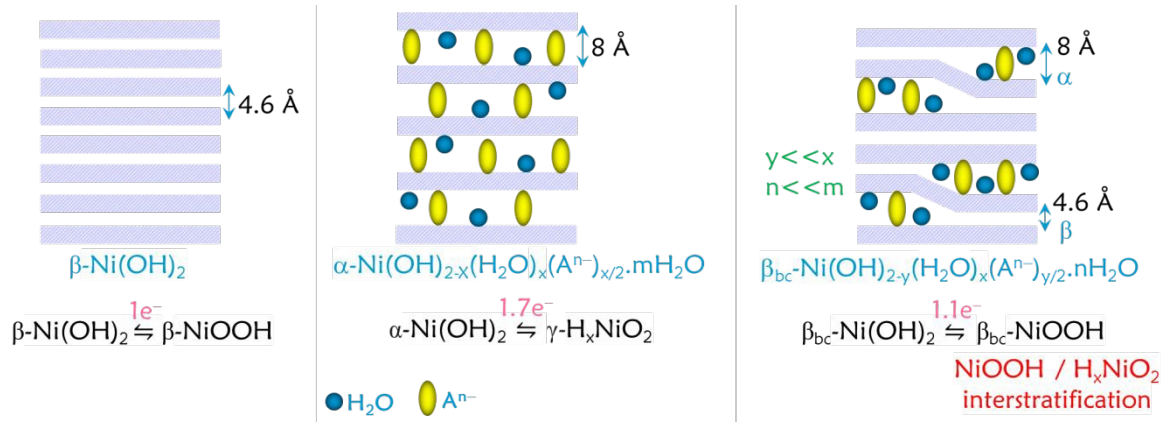

Figure 5 Schematic representations of the structures of the nickel hydroxide polymorphs.

The in-plane HRTEM and Fast Fourier Transform (FFT) analysis of β_{bc}–nickel hydroxide (Figure 4) further establish the coexistence of α and β motifs, and α/β interfaces. Distinct lattice fringes with interlayer spacing of 2.73 and 2.58 Å, indexed to the (100) planes of β–phase and the (111) planes of α-phase respectively indicate the presence of the α and β–motifs in each crystallite. A few regions with fringes due to the (103) planes of α–phase are also observed. Moiré fringes suggest the presence of interstratified layers.

The structure of β_{bc}–nickel hydroxide is schematically shown and compared with the structures of β–nickel hydroxide and α–nickel hydroxide in Figure 5. This schematic also depicts the expected oxyhydroxide phase that would form on oxidation in each of these cases. While β–nickel hydroxide and α–nickel hydroxide would give β–nickel oxyhydroxide (NiOOH) and γ–nickel oxyhydroxide (H_xNiO_2, x=0.25–0.3) respectively, β_{bc}–nickel hydroxide might yield a disordered oxyhydroxide, which is an interstratification of β–nickel oxyhydroxide and γ–nickel oxyhydroxide. This disordered oxyhydroxide may more readily convert to γ–nickel oxyhydroxide compared to the ordered β–nickel oxyhydroxide formed from β–nickel hydroxide.

The OER activity of the nickel hydroxide polymorphs, coated on graphite sheet were evaluated in 1 M KOH. The cyclic voltammetry curves (Figure 6a) obtained at a scan rate of 1 mV s^{-1} indicate quasi reversible redox peaks ascribed to conversion of β and β_{bc}–nickel hydroxide to nickel oxyhydroxide. Both the polymorphs display an oxidation potential of ~1.35 V_{RHE} representing the oxidation of Ni^{2+} to Ni^{3+}/Ni^{4+}, and a second oxidation wave (>1.5 V_{RHE}) attributed to catalytic water oxidation. Similar features are observed in the linear sweep voltammetry (LSV) curves (Figure 6b) recorded at a scan rate of 1 mVs^{-1}. β_{bc}–nickel hydroxide catalyses water oxidation at a lower onset potential of ~1.5 V_{RHE} and delivers higher OER current in comparison to β–nickel hydroxide (Figure 6b). An overpotential of 320 mV at 10 mA cm^{-2} current density (Figure 6b) and a Tafel slope of 60 mV dec^{-1} (Figure 6c), reveal an enhanced oxidation kinetics in the case of β_{bc}–nickel hydroxide compared to β–nickel hydroxide, which shows an overpotential of 380 mV at 10 mA cm^{-2} and a Tafel slope of 95 mV dec^{-1} (Figure 6b and c).

Nyquist plots and the equivalent model of solution resistance (Rs), polarization resistance (Rp) and constant phase element (CPE) are displayed in Figure 6d. The semicircular diameter of β_{bc}–nickel hydroxide is distinctly smaller than that of β–nickel hydroxide indicating a lower charge transfer resistance (R_{ct}) and higher electronic conductivity, thus enabling augmented electrocatalytic activity compared to β–nickel hydroxide and related materials reported in literature (SI, Table S1).

The polymorphic phases were subjected to chronoamperometry at 1.675 V_{RHE}, to gauge their respective stabilities for long-term electrolysis (Figure 6e). In both, β and β_{bc}–phases, the current density increases steadily over a few hours and reaches an equilibrium value which remains constant thereafter. While the β_{bc}–phase delivers a current density of 68 mA cm^{-2}, the β–phase exhibits a relatively lower current density of 47 mA cm^{-2}.

In order to understand the reason for the superior performance of the β_{bc}–phase, the spent electrodes collected under different reaction conditions were analysed using XRD. In the case of β–nickel hydroxide, the XRD pattern (Figure 7A) reveals a weak reflection at ~7 Å along with reflections due to β–$Ni(OH)_2$ under all the reaction conditions. Peak at ~7 Å may be attributed to γ–oxyhydroxide. The intensity of this reflection (in relation to the 001 reflection of β–$Ni(OH)_2$) remains more or less the same at different times of electrolysis. Even the electrode subjected to cyclic voltammetry shows the reflection

View Article Online
DOI: 10.1039/D5LF00195E

at ~7 Å suggesting that the γ–oxyhydroxide is not completely reversible. As the chronoamperometry (Figure 6e) indicates a nearly constant current over 14h, it is fair to assume that γ–oxyhydroxide that is generated at the first reach of the onset potential is involved in the catalysis of the oxygen evolution reaction. In contrast, the β_{bc}–phase (Figure 7B) shows reflections only due to γ–oxyhydroxide even in the case of single sweep LSV and at 1.675 V_{RHE} for all durations. This suggests that the defective β_{bc}–phase with α-motifs convert to γ–oxyhydroxide much more readily than β–nickel hydroxide accounting for its better catalytic activity. In addition, better charge transfer due to defects also contributes to the enhanced efficiency.

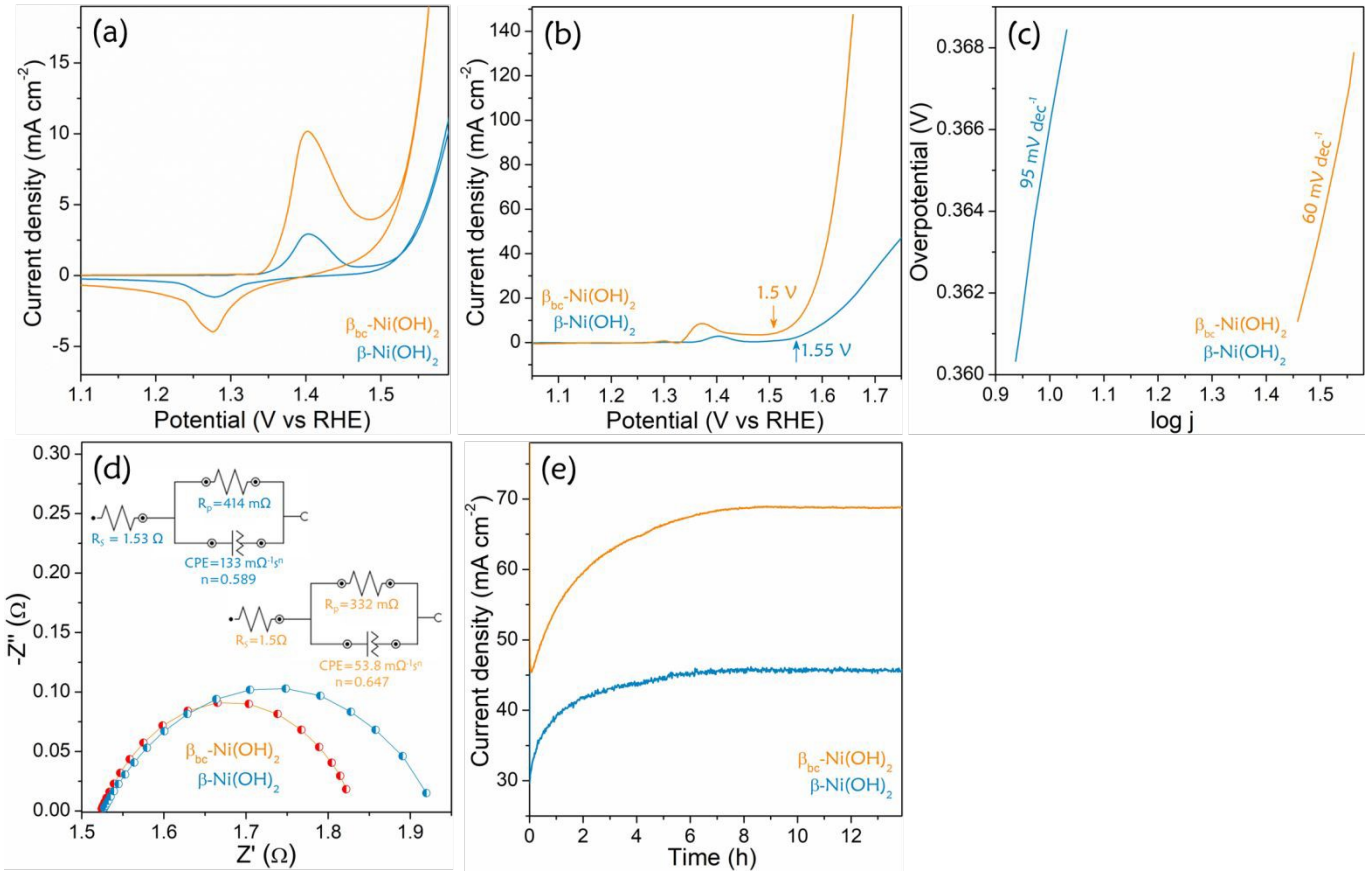

Figure 6 Cyclic voltammograms (a) and LSV recorded at a scan rate of 1 mVs^{-1} in 1 M KOH (b) Tafel plots (η vs log j) (c); Nyquist plots (d); Chronoamperometry (j vs t) at an applied potential of 1.675 V_{RHE} (e) of β and β_{bc}–nickel hydroxide.

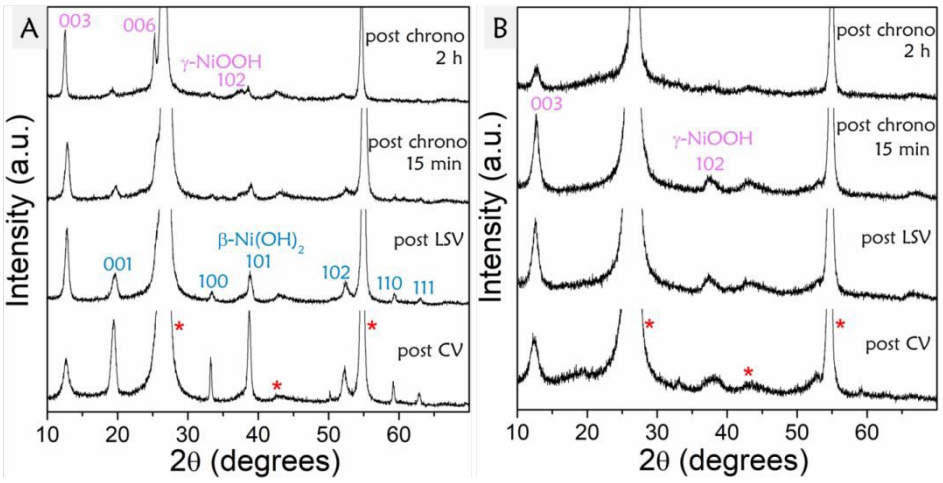

Figure 7 XRD patterns of spent electrodes of (A) β–nickel hydroxide and (B) β_{bc}–nickel hydroxide recorded post CV (50 mVs^{-1}), LSV (5 mVs^{-1}) and chronoamperometry (applied potential 1.675 V_{RHE}) in 1M KOH (OER). Peaks marked as * are due to graphite electrode.

View Article Online
DOI: 10.1039/D6LF00195E

ARTICLE

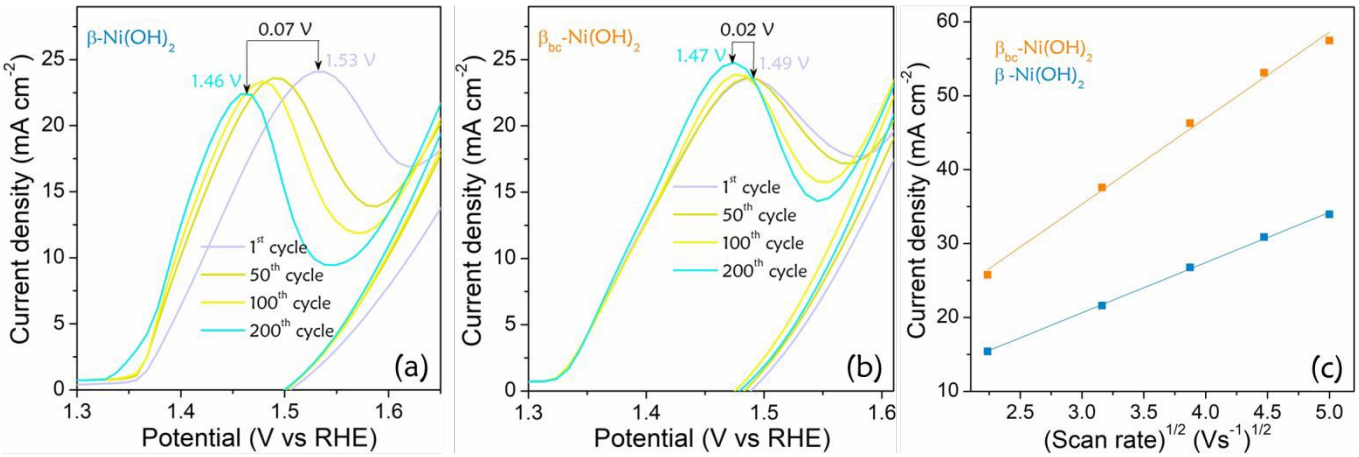

Figure 8 Cyclic voltammograms @10 Vs^{-1} recorded in 1 M KOH (OER) of β–nickel hydroxide (a) and β_{bc}–nickel hydroxide (b); Linear relationship between the anodic peak current density and the square root of the scan rate of β and β_{bc}–nickel hydroxide (c).

It is ideal to identify the catalytic species and the surface reconstruction under operando conditions. Alternatively, the electrode reconstruction maybe understood by carrying out CV over large number of cycles and analyzing the variation of the peak oxidation potential and/or the integrated area under the oxidation curve with the number of cycles. Figure 8a and 8b present the 200 cycle CV data of β and β_{bc}–nickel hydroxide in 1 M KOH respectively. The obvious difference between the two cases is the extent to which the peak oxidation potential (E_p^a) changes with number of cycles. In the case of β–nickel hydroxide E_p^a shifts from 1.53 V_{RHE} in the first cycle to 1.46 V_{RHE} in the 200th cycle indicating a significant modification of the electrode surface. This may be attributed to the catalytic species changing from β–NiOOH to γ–nickel oxyhydroxide. In contrast, a negligible change of E_p^a from 1.49 V_{RHE} to 1.47 V_{RHE} in the case of β_{bc}–nickel hydroxide implies very little modification of the catalytic surface. This further proves that the β_{bc}–phase generates a substantial amount of γ–nickel oxyhydroxide at the onset of OER reaction in comparison to β–nickel hydroxide. The dependance of the peak current on the scan rate is shown in Figure 8c. The slope of the curve for the β_{bc}–phase is approximately twice as much as that of the β–phase indicating a better reconstruction kinetics in the case of the β_{bc}–phase.

The mechanism of phase reconstruction and their catalytic OER activity could be explained as follows. Both β and β_{bc}–nickel hydroxide pre-catalysts undergo reconstruction,[21,22] driven by electrochemical redox reactions, to yield catalytically active β/γ–nickel oxyhydroxide surfaces with higher valency Ni centers. The extent of reconstruction is influenced by the crystallinity and stability of the polymorph and the applied potential.[21,22] At the operational potential of OER (> 1.5 V_{RHE}), nickel hydroxide is prone to get oxidised to γ–nickel oxyhydroxide with $Ni^{3+/4+}$ centres. Cation intercalation is the essential prerequisite for the conversion of the hydroxide to γ–nickel oxyhydroxide.[1,30] While the 12 % α–motifs in the β_{bc} phase initiates the K^+ intercalation, the α/β interfaces and the associated defects help propagate the K^+ insertion in the bulk β matrix, facilitating the formation of γ–nickel oxyhydroxide. In the case of the highly ordered β polymorph, insertion of K^+ is sluggish,[1,30] thus the kinetics of reconstruction to γ–nickel oxyhydroxide is slow. Inherently defective β_{bc} yields γ–nickel oxyhydroxide[31,32,33] with high electrochemical surface area (ECSA) of 118 cm^2 (SI, Figure S2) due to defects,[31,32] vacancies[34,35] and stacking disorder.[33] This is in contrast to 66 cm^2 ECSA of the relatively ordered γ–nickel oxyhydroxide derived from the β polymorph. The formation of defect-rich γ–nickel oxyhydroxide is also evident from the broader reflections in XRD (Figure 7). The FWHM of the 001 reflection of γ–nickel oxyhydroxide formed from β_{bc} and β–phases are 1.1° and 0.36° respectively. Defect-rich γ–nickel oxyhydroxide[36] follows lowest energy pathway at reduced over potential thus exhibiting improved OER activity.[31,32]

The two phases compared here are not of comparable particle sizes. While the β sample is made of thin platelets of ~200 nm diameter, the β_{bc} sample comprise particles of ~20-30 nm diameter. In order to verify if the differences in the observed electrochemical performances of the β and β_{bc}–phases are due to defects and not due to particle size effects, β–nickel hydroxide of comparable particle size as the β_{bc} sample was prepared for comparison. This was achieved by hydrothermal treatment of β_{bc}-nickel hydroxide in 0.2 M KOH at 120 °C for 12 h.

Composition analysis and the XRD pattern (Figure 9a) confirm that the product is β–nickel hydroxide. The SEM image (Figure 9b) of the particles indicate that the sample comprise of particles ~40-50 nm diameter. This ~40 nm β sample exhibits an OER onset potential of 1.54 V_{RHE}, Tafel slope of 112 $mVdec^{-1}$ (SI, Figure S3a and b) and ECSA of 78 cm^2 (SI, Figure S3e), all comparable to the values obtained for the ~200 nm β sample. The chronoamperometric data (Figure 9c)

of this sample is almost the same as that of the 200 nm β sample. These results confirm that the improved performance of the β_{bc}–phase is primarily due to the interstratification and the related defects rather than the decreased particle size.

View Article Online
DOI: 10.1039/D6LF00195E

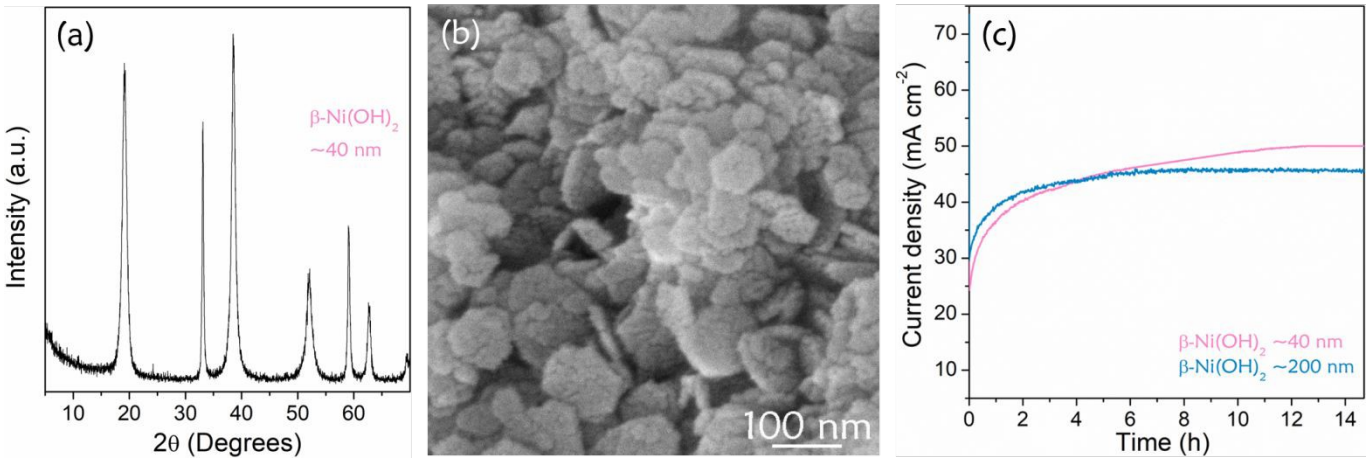

Figure 9. XRD pattern (a); SEM image (b) and Chronoamperometry (j vs t) at an applied potential of 1.675 V_{RHE} (c) of ~40 nm β–nickel hydroxide obtained by hydrothermal treatment of β_{bc}–nickel hydroxide in 0.2 M KOH for 12h.

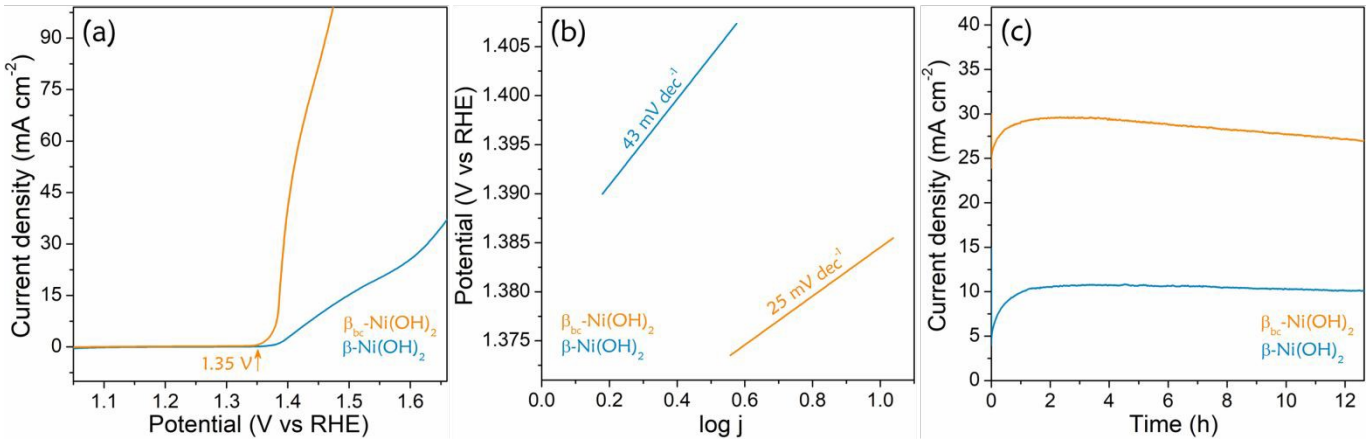

Figure 10 LSV recorded at a scan rate of 5 mV s^{-1} in 1 M KOH with 0.33 M urea (UOR) (a); Tafel plot for UOR (b); Chronoamperometry (j vs t) at an applied potential of 1.4 V_{RHE} in 1M KOH with 0.33M urea (UOR) (c) of β–nickel hydroxide and β_{bc}–nickel hydroxide.

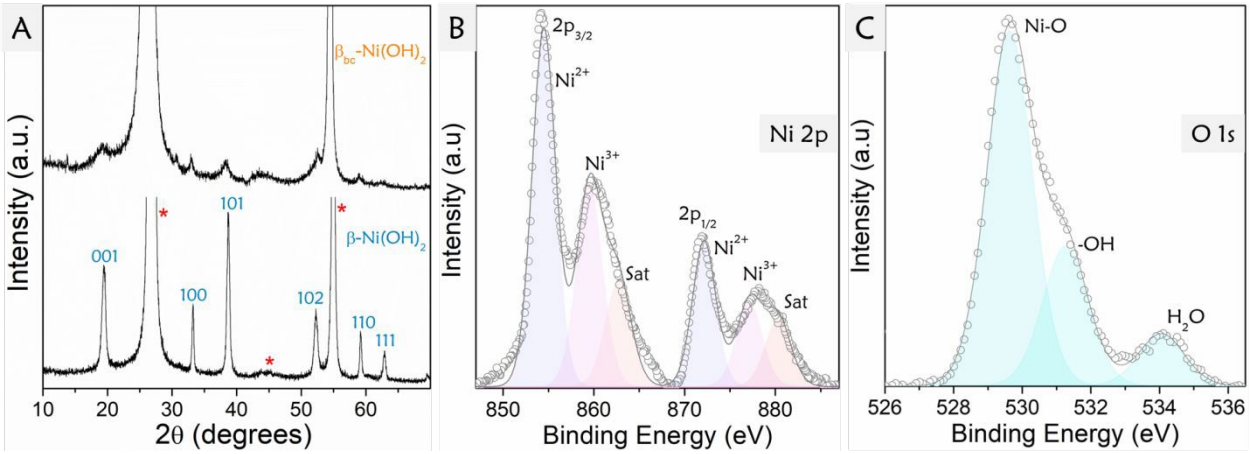

Figure 11 XRD patterns (A) of the spent electrodes of β and β_{bc}–nickel hydroxide post 2h chronoamperometry (applied potential 1.4 V_{RHE}) in 1M KOH with 0.33M urea (UOR). Peaks marked as * are due to graphite electrode. XPS spectra showing Ni 2p (B) and O 1s (C) core-level peak regions of spent electrode of β_{bc}–nickel hydroxide post 2h chronoamperometry (UOR).

View Article Online
DOI: 10.1039/D6LF00195E

ARTICLE

Electrocatalytic oxidation of typical organic pollutants is explored as an alternative to the anodic OER to mitigate the cell potential of electrocatalytic hydrogen generation.[37,38] Urea is one of the targeted compounds.[37,38] Nickel hydroxide based electrocatalysts have been tested for urea oxidation reaction (UOR).[34,39-51] Chakrabarty et al[49] have suggested that when α/β-mixed nickel hydroxides were employed as UOR electrocatalysts the efficiency increases with the α-phase content and this is attributed to the formation of γ–oxyhydroxide. However, it is fairly well established that the active catalytic species for UOR is β-NiOOH, as the onset of UOR almost coincides with $Ni^{2+} \rightarrow Ni^{3+}$ oxidation.[52-54] In order to verify if indeed γ–oxyhydroxide catalyses UOR, electrocatalytic UOR activity of β_{bc}–phase was analysed.

β_{bc}–nickel hydroxide displays an onset potential of 1.35 V_{RHE} which is 140 mV lower compared to the onset potential for OER. A current density of 10 mA cm^{-2} is achieved at 1.38 V_{RHE} (Figure 10a) with a Tafel slope of 25 mV dec^{-1} (Figure 10b). The chronoamperometric j-t curve (Figure 10c) of β_{bc}–nickel hydroxide exhibits appreciable stability towards UOR, delivering an average current density of 26.5 mA cm^{-2} (1.4 V_{RHE}) over 13 h. With these attributes the β_{bc} polymorph is as good as or better than the nickel hydroxide based electrocatalysts reported in the literature (SI, Table S2). In comparison, β–nickel hydroxide exhibits an onset potential, potential at 10 mA cm^{-2} and Tafel slope of 1.39 V_{RHE}, 1.46 V_{RHE} and 43 mV dec^{-1} respectively (Figure 10). These results suggest that β_{bc}–nickel hydroxide is better than β–nickel hydroxide in UOR catalysis too. Here again, the electrocatalytic UOR activity (SI, Figure S3) of ~40 nm β sample with ECSA of 105 cm^{-2} is comparable to the activity exhibited by the ~200 nm β sample.

To identify the active catalytic species in UOR, the spent electrodes of both β and β_{bc}–nickel hydroxide under various reaction conditions were characterized using XRD. In both the cases, under all conditions, the XRD pattern (Figure 11A) of the spent electrodes shows reflections due to β–nickel hydroxide only, thus indicating that γ–nickel oxyhydroxide is not involved in UOR catalysis. The presence of β–NiOOH in the spent electrodes could not be ascertained by XRD analysis.[53] Therefore, the spent electrodes recovered after 2h of UOR at 1.4 V_{RHE} were subjected to XPS analysis (Figure 11B and C). The core-level Ni 2p spectrum (Figure 11B) of β_{bc}-nickel hydroxide subjected to UOR exhibits a doublet $2p_{3/2}$ and $2p_{1/2}$ due to spin-orbit coupling along with satellite peaks. While the peaks at 854.44 and 872.02 eV are due to Ni^{2+}, the peaks at 859.62 and 877.03 eV are due to Ni^{3+} species. The relative concentration (peak intensity) of Ni^{3+} is found to be 60% validating β-NiOOH to be the active catalytic phase in UOR. The presence of surface-hydrated oxides and (oxy)hydroxide phases during the catalytic UOR is also corroborated by the presence of peaks at 531.28 and 534.12 eV along with lattice oxygen at 529.6 eV in the core-level O 1s spectrum (Figure 11c).

Nickel hydroxide undergoes dynamic surface reconstruction during electrochemical UOR process.[21,22,54] At the low operational potential of UOR ~1.4 V_{RHE}, nickel hydroxide is oxidised to β-NiOOH with Ni^{3+} centres. UOR at β-NiOOH has been shown to follow either direct or indirect mechanism.[50-54] The indirect pathway involves oxidation of urea and simultaneous reduction of β-NiOOH to β-$Ni(OH)_2$ and catalysis is sustained by the regeneration kinetics of β-NiOOH. The direct UOR mechanism conserves the β-NiOOH active surface while urea is oxidised. Though desired, the direct route requires abundant Ni^{3+} centres. Degradation of current density in both the pathways is attributed to CO_x poisoning of the active surface.[50-54]

Regeneration kinetics of β–NiOOH determines the stability and efficiency of the catalyst. β_{bc}–phase yields disordered β–NiOOH with higher ECSA (145 cm^2) compared to 98.8 cm^2 of ordered β–NiOOH derived from the β–phase (SI, Figure S4). Presence of ordered β–$Ni(OH)_2$ post chronoamperometry (Figure 11A) indicates rapid consumption of the ordered β–NiOOH and the kinetically hindered regeneration during UOR. In contrast, the shallow and broad reflections in XRD (Figure 11A), and 60% Ni^{3+} observed in XPS (Figure 11B) post chronoamperometry in the case of β_{bc}–phase suggest rapid consumption-regeneration of the active disordered β–NiOOH. Hence, the β_{bc}–phase delivers higher current density at lower potentials for UOR.

The failure of XRD and XPS in detecting the presence of Ni^{4+} species in the spent electrodes may not completely rule out the role of γ–nickel oxyhydroxide as a catalytic species in UOR in the case of β_{bc}–nickel hydroxide. The ordered β–nickel hydroxide would involve β–NiOOH as the only catalytic species at the low potentials (<1.4 V_{RHE}) at which UOR occurs. Even at these potentials, β_{bc}–nickel hydroxide would reconstruct into β_{bc}–nickel oxyhydroxide, which is an interstratification of β and γ (~12%) oxyhydroxide motifs (Figure 5). This small percentage of the γ–oxyhydroxide motifs could be the reason behind the much-enhanced electrocatalytic activity of β_{bc}–nickel hydroxide compared to β–nickel hydroxide in UOR. Unlike in the case of OER, the Ni^{4+} species is consumed by the reactant, urea, as quickly as it is formed leading to its absence in the spent electrode.

The ease of formation of active β–NiOOH is further ascertained from the CV data at different scan rates. The anodic peak current density increases with the scan rate in both the phases (Figure 12) resulting in a linear relation with the square root of the scan rate. The observed slope for the β_{bc}–phase is ~2.5 times that the formation of the electroactive oxyhydroxide for the UOR process. of the β–phase, indicating enhanced diffusivity of hydroxyl ions promoting

View Article Online
DOI: 10.1039/D6LF00195E

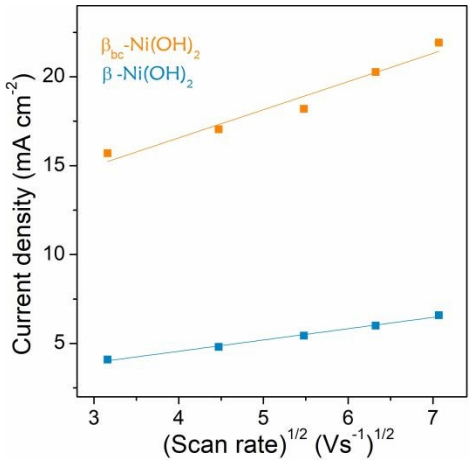

Figure 12 Linear relationship between the anodic peak current density and the square root of the scan rate of β and β_{bc}–nickel hydroxides.

Conclusions

As anticipated, β_{bc}–nickel hydroxide performs better than the β–polymorph in the electrocatalysis of OER. The coexistence of α–motifs (~12%) along with β–motifs is the reason for augmented performance of the β_{bc} polymorph. XRD studies of the spent electrodes suggest that the active catalytic species for OER is γ–nickel oxyhydroxide. In the case of β_{bc}–nickel hydroxide the γ–nickel oxyhydroxide conversion is initiated in the α–motifs and propagated across the crystallite through the α/β interfaces. This conversion is sluggish and partial in the case of β–nickel hydroxide leading to its poorer performance. Even in the case of UOR, where the active catalytic species is β–NiOOH, β_{bc}–nickel hydroxide shows enhanced performance compared to the β–polymorph due to its defective structure offering better charge transfer and also due to the possible formation of γ–nickel oxyhydroxide as the catalytic species.

Conflicts of interest

There is no conflict of interest.

Acknowledgements

Support by DST-FIST funding (SR/FST/College-324/2016) for the procurement of Simultaneous Thermal Analyzer is acknowledged.

References

1 P. Oliva, J. Leonardi, J. F. Laurent, C. Delmas, J. J. Braconnier, M. Figlarz, F. Fievet and A. de Guibert, *J. Power Sources,* 1982, **8**, 229.
2 M. Rajamathi, G. S. Thomas and P. V. Kamath, *J. Chem Sci.,* 2001, **113**, 671.
3 D. S. Hall, D. J. Lockwood, C. Bock and B. R. MacDougall, *Proc. R. Soc. A,* 2014**, 471**: 20140792.
4 C. Delmas, C. Faure, L. Gautier, L. G.-Demourgues and A. Rougier, *Phil. Trans. Roy. Soc. Lond*. A, 1996, **354**, 1545.
5 C. Nethravathi, N. Ravishankar, C. Shivakumara and M. Rajamathi, *J. Power Sources,* 2007, **172**, 970.
6 L. Feng, Y. Zhu, H. Ding and C. Ni, *J. Power Sources,* 2014, **267**, 430.
7 M. Sebastian, C. Nethravathi and M. Rajamathi, *Mater. Res. Bull.,* 2013, **48**, 2715.
8 M. Rajamathi, P. V. Kamath and R. Seshadri, *J. Mater. Chem.*, 2000, **10**, 503.
9 M. Rajamathi, G. N. Subbanna and P. V. Kamath, *J. Mater. Chem.,* 1997, **7**, 2293.
10 P. H. Ho, I. Z. Awan, N. Tanchoux, R. Arletti, S. Albonetti, F. Cavani, A. Martucci, H. Petitjean, D. Tichit, P. Benito and F. Di Renzo, *J. Mater. Sci.,* 2025, **60**, 5019.
11 V. Vij, S. Sultan, A. M. Harzandi, A. Meena, J. N. Tiwari, W. G. Lee, T. Yoon and K. S. Kim, *ACS Catal.*, 2017, **7**, 7196.
12 G. Chen, H. Wan, W. Ma, N. Zhang, Y. Cao, X. Liu, J. Wang and R. Ma, *Adv. Energy Mater*., 2019, 1902535.
13 M. Gao, W. Sheng, Z. Zhuang, Q. Fang, S. Gu, J. Jiang and Y. Yan, *J. Am. Chem. Soc.,* 2014, **136**, 7077.
14 P. Tian, Y. Yu, X. Yina and X. Wang, *Nanoscale,* 2018, **10**, 5054.
15 L.-A. Stern and X. Hu, *Faraday Discussions,* 2014, **176**, 363.
16 X. P. Wang, H. J. Wu, S. B. Xi, W. S. V. Lee, J. Zhang, Z. H. Wu, J. O. Wang, T. D. Hu, L. M. Liu, Y. Han, S. W. Chee, S. C. Ning, U. Mirsaidov, Z. B. Wang, Y. W. Zhang, A. Borgna, J. Wang, Y. H. Du, Z. G. Yu, S. J. Pennycook and J. M. Xue, *Energy Environ. Sci.*, 2020, **13**, 229.
17 X. Zhou, Z. Xia, Z. Zhang, Y. Ma and Y. Qu, *J. Mater. Chem. A*, 2014, **2**, 11799.
18 D. Lim, S. Kim, N. Kim, E. Oh, S. E. Shim and S.-H. Baeck, *ACS Sustainable Chem. Eng*., 2020, **8**, 4431.
19 R. Subbaraman, D. Tripkovic, K.-C. Chang, D. Strmcnik, A. P. Paulikas, P. Hirunsit, M. Chan, J. Greeley, V. Stamen Kovic and N. M. Markovic, *Nat. Mater.*, 2012, **11**, 550.
20 K. Zhu, H. Liu, M. Li, X. Li, J. Wang, X. Zhu and W. Yang, *J. Mater. Chem. A*, 2017, **5**, 7753.
21 H. Chen, L. Wang, M. Na and X. Zou, *Chem. Sci.*, 2025, **16**, 20662.
22 J. Feng, X. Wang and H. Pan, *Adv. Mater.*, 2024, **36**, 2411688.
23 Z. Shen, K. Wang, Y. Yuan, F. Gao, X. Wang, W. Cui, F. Qi, X. Ren, J. Chen, C. Xiao and H. Pan, *Small Methods*, 2025, **9**, 2500736.
24 R. I. Bickley, T. G. Carreno, J. S. Lee, L. Palmisano and R. J. D. Tilley, *J. Solid State Chem*., 1991, **92**, 178.
25 Y. Zhang, Y. Kuwahara, K. Mori, C. Louis and H. Yamashita, *Nanoscale*, 2020, **12**, 11908.
26 G. Mineo, M. Scuderi, E. Bruno and S. Mirabella, *ACS Appl. Energy Mater.*, 2022, **5**, 9702.
27 S. Anantharaj and S. Noda, *J. Mater. Chem. A*, 2022, **10**, 9348.
28 M. M. J. Treacy, J. M. Newsam and M. W. Deem, Proc. R. Soc. London A, 1991, 433, 499.
29 M. C. Bernard, R. Cortes, M. Keddam, H. Takenouti, P. Bernard and S. Senyarich, *J. Power Sources*, 1996, **63**, 247.
30 D. K. Bediako, B. L.-Kaiser, Y. Surendranath, J. Yano, V. K. Yachandra and D. G. Nocera. *J. Am. Chem. Soc.,* 2012, **134**, 6801.
31 L.-F. Li, Y.-F. Li and Z.-P. Liu. *ACS Catal*. 2020, **10**, 2581.
32 P. W. Menezes, S. Yao, R. B.-Suito, J. N. Hausmann, P. V. Menezes and M. Driess. *Angew. Chem. Int. Ed.,* 2021, **60**, 4640.
33 J. Kang, Y. Xue, J. Yang, Q. Hu, Q. Zhang, L. Gu, A. Selloni, L.-M. Liu and L. Guo. *J. Am. Chem. Soc.,* 2022, **144**, 8969.

View Article Online
DOI: 10.1039/D6LF00195E

34 Q. He, Y. Wan, H. Jiang, Z. Pan, C. Wu, M. Wang, X. Wu, B. Ye, P. M. Ajayan and L. Song. *ACS Energy Lett*., 2018, **3**, 1373.
35 D. Yan, C. Xia, W. Zhang, Q. Hu, C. He, B. Y. Xia and S. Wang, *Adv. Energy Mater*., 2022, 2202317.
36 S. Qi, J. You, X. Liufu, Y. Zhang, R. Chen, J. Zhuang, T. Liang, L. Li, Q. Huo, C. Shang, X. Zhang, H. Yang, Q. Hu and C. He. *Adv. Mater.,* 2026, **38**, e12188.
37 S. Ghosh, D. Bagchi, I. Mondal, T. Sontheimer, R. V. Jagadeesh and P. W. Menezes, *Adv. Energy Mater.,* 2024, **14**, 2400696.
38 J. Liu, Y. Du, D. Zheng, S. Wang, Y. Hou, J. Zhang and X. F. Lu, *ACS Materials Lett.*, 2024, **6**, 466.
39 Q. Li, J. Wang, Y. Shi, H. Li, H. Yang, K. Xiang, W. You and J. Liang, *Mater. Horiz.,* 2025, **12**, 9952.
40 W. Yang, X. Yang, C. Hou, B. Li, H. Gao, J. Lin and X. Luo, *Appl. Catal. B*, 2019, **259**, 118020.
41 J. Xie, W. Liu, X. Zhang, Y. Guo, L. Gao, F. Lei, B. Tang and Y. Xie, *ACS Materials Lett.*, 2019, **1**, 103.
42 J. Chen, S. Ci, G. Wang, N. Senthilkumar, M. Zhang, Q. Xu and Z. Wen, *ChemElectroChem*, 2019, **6**, 5313.
43 C. Lin, Z. Gao, F. Zhang, J. Yang, B. Liu and J. Jin, *J. Mater. Chem. A,* 2018, **6**, 13867.
44 H. Qin, Y. Ye, J. Li, W. Jia, S. Zheng, X. Cao, G. Lin and L. Jiao, *Adv. Funct. Mater.,* 2023, **33**, 2209698.
45 X. Zhu, X. Dou, J. Dai, X. An, Y. Guo, L. Zhang, S. Tao, J. Zhao, W. Chu, X. C. Zeng, C. Wu and Y. Xie, *Angew. Chem., Int. Ed.,* 2016, **55**, 12465.
46 L. Zhang, L. Wang, H. Lin, Y. Liu, J. Ye, Y. Wen, A. Chen, L. Wang, F. Ni, Z. Zhou, S. Sun, Y. Li, B. Zhang and H. A. Peng, *Angew. Chem., Int. Ed.,* 2019, **58**, 16820.
47 Z. Zheng, D. Wu, L. Chen, S. Chen, H. Wan, G. Chen, N. Zhang, X. Liu and R. Ma, *Appl. Catal. B*, 2024, **340**, 123214.
48 W. Yang, X. Yang, B. Li, J. Lin, H. Gao, C. Hou and X. Luo, *J. Mater. Chem. A,* 2019, **7**, 26364.
49 S. Chakrabarty, I. O.-Polak, T. Y. Burshtein, M. E. Farber, L. Kornblum and D. Eisenberg, *J. Solid State Electrochem.*, 2021, **25**, 159.
50 L. Sun, X. Li, J. Li, Y. Zeng, and S. Lu, *Energy Fuels* 2025, **39**, 13969.
51 Y. Zeng, S. Xiang, S. Lu, and X. Qi, *Materials* 2024, **17**, 2617.
52 V. Vedharathinam and G. G. Botte, *J. Phys. Chem. C*, 2014, **118**, 21806.
53 D. Wang and G. G. Botte. *ECS Electrochem. Lett.*, 2014, **3**, H29.
54 W. Li, X. Lu and Z. Li, *Adv. Energy Mater.,* 2026, **16**, e04716.

Data Availability Statement

α and β–motifs Interstratified β_{bc}–Nickel Hydroxide for Enhanced OER and UOR Electrocatalysis

C. M. Avinash,[1] C. Nethravathi[1,2] Michael Rajamathi[1*]*

[1]Materials Research Group, St. Joseph's University, 36 Lalbagh Road, Bangalore 560027, India
[2]Department of Chemistry, Mount Carmel College, 58 Palace Road, Vasanth Nagar, Bangalore 560052, India
Corresponding Author.
Email: michael.rajamathi@sju.edu.in; nethravathic@gmail.com

All the data supporting this article have been included in the manuscript and in the Supplementary Information.